Gabriel Dan Ciocan
Research Associate
e-mail: gabrieldan.ciocan@orange.fr

Monica Sanda Iliescu
Doctoral Student
e-mail: msiliescu@yahoo.fr

Laboratory for Hydraulic Machines,
Ecole Polytechnique Fédérale de Lausanne
(EPFL),
Avenue de Cour 33bis,
CH-1007, Lausanne, Switzerland

Thi Cong Vu
Senior Developement Engineer
e-mail: thi.vu@ps.ge.com

Bernd Nennemann
Research Assistant
e-mail: bernd.nennemann@ps.ge.com

Hydropower Technology,
GE Energy,
795 George V,
Lachine, Quebec, H8S-4K8, Canada

François Avellan
Professor
Laboratory for Hydraulic Machines,
Ecole Polytechnique Fédérale de Lausanne
(EPFL),
Avenue de Cour 33bis,
CH-1007, Lausanne, Switzerland
e-mail: francois.avellan@epfl.ch

Experimental Study and Numerical Simulation of the FLINDT Draft Tube Rotating Vortex

The dynamics of the rotating vortex taking place in the discharge ring of a Francis turbine for partial flow rate operating conditions and cavitation free conditions is studied by carrying out both experimental flow survey and numerical simulations. 2D laser Doppler velocimetry, 3D particle image velocimetry, and unsteady wall pressure measurements are performs to investigate thoroughly the velocity and pressure fields in the discharge ring and to give access to the vortex dynamics. Unsteady RANS simulation are performed and compared to the experimental results. The computing flow domain includes the rotating runner and the elbow draft tube. The mesh size of 500,000 nodes for the 17 flow passages of the runner and 420,000 nodes for the draft tube is optimized to achieve reasonable CPU time for a good representation of the studied phenomena. The comparisons between the detailed experimental flow field and the CFD solution yield to a very good validation of the modeling of the draft tube rotating vortex and, then, validate the presented approach for industrial purpose applications.
[DOI: 10.1115/1.2409332]

1 Introduction

Hydropower is a clean form of power generation, which uses a renewable source of energy: water. Moreover, storage capability and flexible generation makes hydropower the quasi-ideal form of power generation to meet the variable demand of the electricity market, therefore it is not surprising that the turbines tend to be operated over an extended range, far from the optimum flow conditions. In particular, at part load operating conditions turbine fixed-pitch runners show a strong swirl at the runner outlet. As the incoming swirling flow is decelerating in the diffuser cone, a hydrodynamic instability arises under the form of a characteristic precession flow—see Jacob [1].

For the usual setting levels of the turbines, defined by the Thoma cavitation number σ, the static pressure is such that the cavitation development makes visible the core of the vortex and, therefore, the precession movement through a typical helical shape of the cavity in the draft tube cone. The cavitation vortex core of the swirling flow at the runner outlet is the so-called "rope." The development of cavitation introduces compliance in the turbine draft tube flow and, consequently, a natural frequency corresponding in a first approximation to the frequency of the free oscillation of the water plug in the draft tube against the compliant

vapors volume of the rope. The coupling between this natural frequency and the precession frequency leads to the draft tube surge; see Nishi et al. [2], which can inhibit the operation of the whole hydropower plant.

Characterizations of the part load operating conditions have been carried out extensively; see Jacob [1], and the technology for overcoming the draft tube surge through active control has been established. However, any attempt of modeling the hydrodynamic phenomena leading to the development of the rope and its interaction with all the turbine and hydraulic system components needs further investigations.

Recent developments of experimental methods and numerical simulation techniques permit the detailed analysis of this flow. It is feasible presently to predict this operating regime, from the point of view of the theoretical background, the computational resources, and the existence of accurate experimental measurements to rely on.

The availability of advanced optical instrumentation, such as laser Doppler velocimetry (LDV) or particle image velocimetry (PIV) systems, gives the opportunity to perform flow surveys in turbomachinery and in particular to investigate the unsteady characteristics of the complex flow velocity fields in the case of, for instance, the rotor-stator interactions, the draft tube, or the spiral casing.

The progress of the numerical techniques in the prediction of the turbine characteristics for the operating ranges in the vicinity of the beam efficiency point (BEP) insure a good accuracy—see

---

Copyright © 2007 by ASME

Table 1 Bibliographical result of the CFD/experimental global values comparison

Comparison between experimental and numerical data	Ruprecht et al.[a]	Scherer et al.[b]	Miyagawa et al.[c]	Sick et al.[d]	This paper
CFD f_r/Experimental f_r	0.93	1 (low resolution)	Not available	1.12	1.13
CFD pressure pulsation amplitude/experimental pressure pulsation amplitude	0.7–1.3	1–1.4	Not available	0.83	1

[a]See Ref. [5].
[b]See Ref. [6].
[c]See Ref. [7].
[d]See Ref. [8].

Vu et al. [3]. The massively parallel computations development permits now the numerical simulation of the whole turbine—see Ruprecht et al. [4] or to detail the flow in a specific part of the turbine.

One of the new challenges for the numerical turbine simulation is to predict the partial or full flow rate operating regimes and the first simulations are promising. Ruprecht et al. [5] are focused on the influence of different turbulence models on the modeling of the draft tube vortex, carried out in a straight cone. Based on the length of the predicted vortex structure, certain turbulence models tend to have a damping effect and from this point of view, the most accurate, is found to be a two-scale model described by Hanjalic, reduced to a two equations set by a Very Large Eddy Simulation (VLES) approach. The validation of the numerical simulation is performed on a Francis turbine draft tube with three outlet channels. For a relatively coarse mesh—250,000 nodes—and the computed runner outlet velocity profile as inlet conditions, the vortex frequency is well predicted—93% of the measured vortex frequency, but an underestimation of the wall pressure fluctuation amplitudes is obvious. The given explanation turns towards the possible variation of the flow rate during operation at low flow rate.

Scherer et al. [6] reported the turbine design improvement for the draft tube operating at partial flow rate conditions by Computational Fluid Dynamics (CFD). An unsteady one-phase Reynold's Averaged Navier-Stokes (RANS) simulation of the draft tube vortex in a Francis turbine model is used to compare two draft tube configurations. By comparing the calculated performances of two model machines over the operating range, the second one is found to have better draft tube efficiency at low flow rate operation, justified by the obtained pressure pulsations improvement, the diminishing of the strong velocity gradients, and backflow zone in the cone. The comparison with wall pressure experimental data shows a good agreement for the vortex frequency and a systematic underestimation of the pressure fluctuation amplitudes.

Miyagawa et al. [7] performed an unsteady simulation of the draft tube vortex for a Francis pump turbine, consecutively for two different runners. The purpose was to analyze the influence of the velocity profile at the runner outlet on the flow instability in the draft tube. Two runner designs are tested for the same draft tube geometry—using a mesh of 620,000 nodes. The same vortex behavior changes are observed in CFD and experimentally by qualitative comparisons with the rope visualizations. The authors tested a one phase and a two-phase model as well, and found that it influences mainly the fluctuation amplitude and has no influence on the vortex frequency, but no further details are given. The void fraction in the vortex core is found to be similar compared to high-speed camera visualizations, but quantitative comparisons are not available.

In the last two papers, the inlet boundary conditions are taken as the result of the steady calculation of the runner and/or guide vanes—stay vanes. It provides, thus, the uniform axial and tangential velocity profile, circumferentially averaged. As outlet condition, a constant pressure value is considered.

Sick et al. [8] performed a numerical simulation of a pump turbine with a Reynolds stress turbulence model, already validated for near BEP operating conditions. Unlike other studies, the runner and the outlet domain were included in the computational domain with 1.5 million of cells for minimizing the steady inlet velocity profile effect and the uniform outlet pressure boundary condition effect. The comparison with experimental data shows an overestimation of the vortex frequency and a quite good agreement for the pressure fluctuations amplitude. The analysis of the forces and bending moments on the runner shaft due to the vortex gives the same characteristics like the pressure pulsations: a good agreement for the amplitude and an overestimation of the frequency.

These papers get to a fairly good agreement with the global characteristics of the flow—see Table 1, but a validation implies the validations of the partial flow rate vortex phenomenology and also comparisons of the detailed flow field.

In the frame of the FLINDT—flow investigations in draft tubes—project, Eureka No. 1625, the operation in low flow rate conditions of a Francis turbine is investigated, both experimentally and numerically.

The present paper describes:

— FLINDT phase 2 experimental LDV, PIV, and wall pressure measurements for the rotating vortex study in noncavitating regime in the cone of the draft tube. In this paper only the local measurements in the cone region will be presented;
— CFD methodology for the unsteady simulation of the rotating vortex;
— comparison of the numerical solution with experimental data.

2 Experimental Approach for the Draft Tube Rotating Vortex Measurement Scale Model of Francis Turbine

The investigated case corresponds to the scale model of the Francis turbines of high specific speed, $\nu=0.56$ ($n_q=92$) of a hydropower plant built in 1926, owned by ALCAN. The 4.1 m diameter runners of the machines were upgraded in the late 1980s. The original draft tube geometry is of Moody type. For the purpose of the FLINDT research project, an especially designed elbow draft tube with one pier replaces the original Moody draft tube. The scale model—$\bar{D}_{1e}=0.4$ m—is installed on the third test rig of the EPFL Laboratory for Hydraulic Machines and the tests are carried out according to the IEC 60193 standards [9].

The energy-flow coefficients and efficiency characteristics of the scale model are represented on the hill chart in Fig. 1. According to the objective of the study, an operating point is selected at partial flow rate condition. The point of interest is selected for a specific energy coefficient of $\psi=1.18$ and a flow rate coefficient of $\varphi=0.26$, which corresponds to about 70% Q_{BEP} and a Re number of 6.3×10^6.
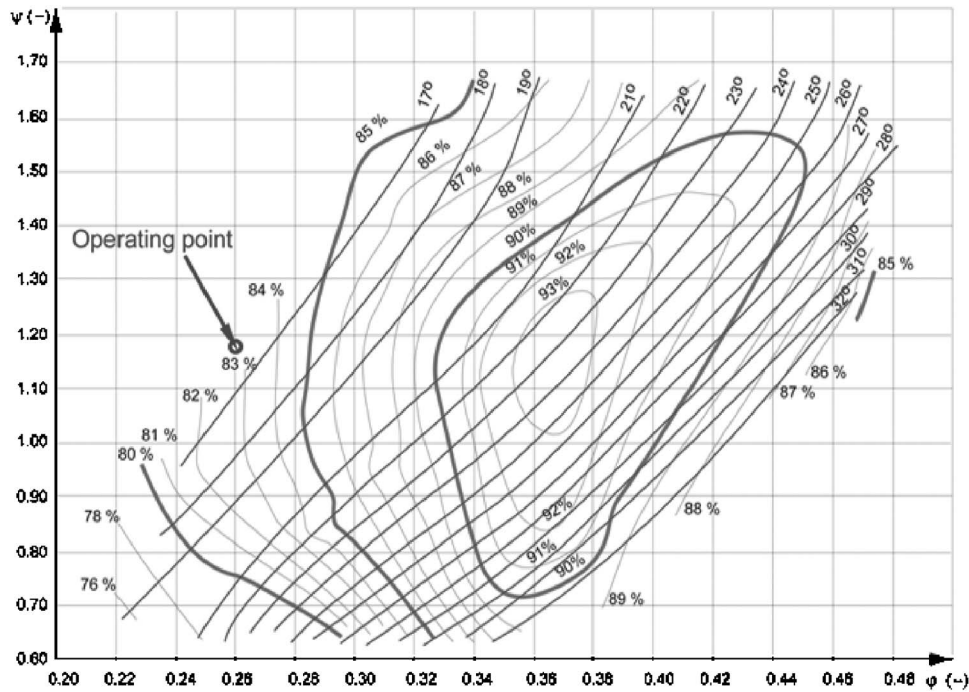
Fig. 1 Scale model hill chart and part load operating point

Three different measurement methods are used: 3D PIV, 2D LDV, and unsteady wall pressure. The investigated zones are presented in Fig. 2.

2.1 Particle Image Velocimetry Instrumentation. The 3D instantaneous velocity field in the cone is investigated with a Dantec M.T. 3D PIV system, which consists of a double-pulsed laser, two double-frame cameras, and a processor unit for the acquisition synchronization and the vectors detection by cross correlation.

The illuminating system is composed of two laser units with Neodynium-doped Yttrium Aluminium Garnet crystals (Nd:YAG), each delivering a short impulse of 10 ns and 60 mJ energy at 8 Hz frequency. Thus the time interval between two successive impulses can easily be adjusted within $1~\mu s - 100$ ms range, depending on the local flow characteristics or the phenomenon, which is to be captured. The output laser beam of 532 nm is guided through an optical arm, for accessibility, to a beam expander and transformed into a sheet of 4 mm width and 25 deg divergence.

Two Hi-Sense cameras with a resolution of 1280×1024 pixels are used for 200×150 mm^2 investigation area. The cameras are placed in a stereoscopic configuration, focused on the laser-sheet, synchronized with the two pulses. They capture the position of seeding particles of $\sim 10~\mu m$ diameter by detecting their scattered light. In order to avoid possible reflections in the laser wavelength on the cameras, due to the optical interfaces or to residual bubbles in the flow, fluorescent particles of 580 nm emission wavelength are used, along with corresponding cutoff filters on the cameras.

For the optical access, the cone is manufactured in Polymethyl methacrylate (PPMA) with a refractive index of 1.4, equipped with a narrow window for the laser's access and two large symmetric windows for the cameras access, having a flat external surface for minimizing the optical distortions.

The corresponding two-dimensional vector maps, obtained from each camera by a fast Fourier transform-based algorithm, are combined in order to have the out-of-plane component, character-
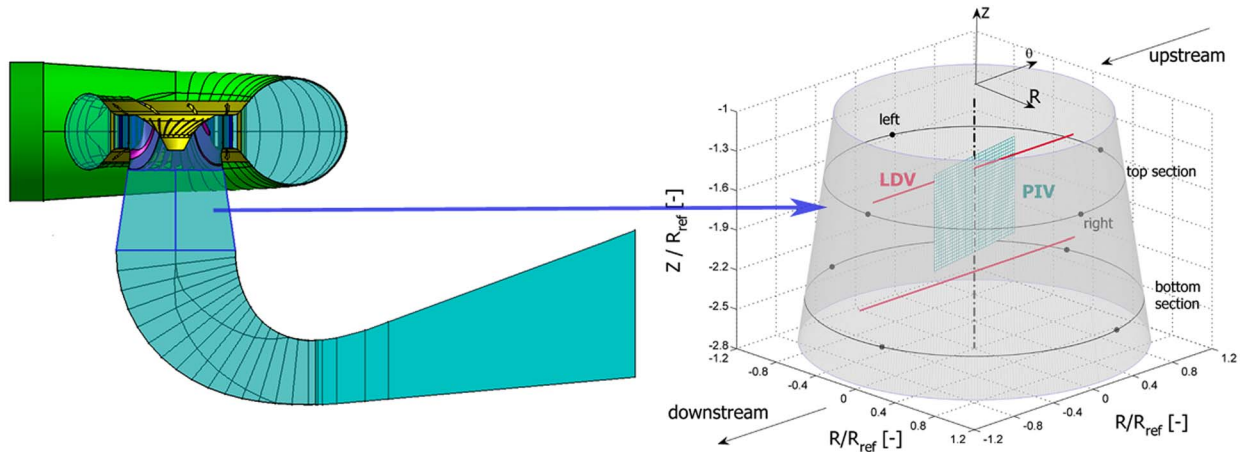

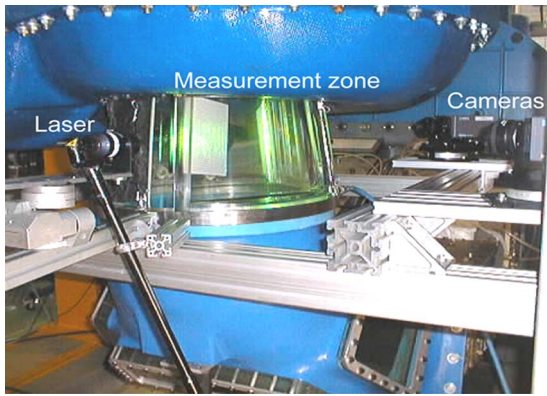**Fig. 2 Measurement zones in the cone of the FLINDT turbine**

Fig. 3 Calibration setup for 3D PIV measurements

izing the displacement in the laser-sheet width.

The correlation between the local image coordinates and real space coordinates is realized through a third order optical transfer matrix, which includes the correction of distortions due to different refractive indices in the optical path and to the oblique position of the cameras. The calibration relation is obtained acquiring images of a plane target with equally spaced markers, moved in five transversal positions in order to have volume information, see Fig. 3. The target displacement in the measurement zone, with accuracy within the narrow limits of 0.01 mm in translation and 0.1 deg in rotation, insured a good calibration quality; see Iliescu et al. [10]. The overall uncertainty of the PIV 3D velocity fields is 3% of the mean velocity value.

2.2 Laser Doppler Velocitry Instrumentation. The 2D velocity profile survey is performed by the LDV measurement method—see Fig. 2, on two complete diameters, at the cone inlet and outlet.

The LDV system is a Dantec M.T. two components system, using backscattered light and transmission by optical fiber, with a laser of 5 W argon-ion source. An optical window with plane and parallel faces is used as interface. The geometrical reference position of the measurements is obtained by positioning the laser beams on the windows faces with accuracy better than 0.05 mm. Two components are measured: the tangential component of the velocity C_u and the axial one C_z, see Fig. 2. The uncertainties of the laser measurements are estimated to 2%—see Ciocan et al. [11].

2.3 Unsteady Wall Pressure Instrumentation. The unsteady wall pressure measurements—100 simultaneous acquisitions—

permit to discriminate the rotating pressure field due to the vortex rotation and the synchronous pressure field at the same frequency—see Arpe. [12] In order to capture the phenomena of interest in low flow rate turbine operating conditions, all pressure signals are acquired simultaneously with a HP-VXI acquisition system using a sampling frequency of $16 \times n$, $80 \times n$ and 2^{14} samples. The spectral analysis does not show differences between the three sampling frequencies, thus for the analysis it was chosen the $16 \times n$ acquisition rate. This setup allows recording 430 vortex passages, providing an acceptable number of segments for the averaging process and insuring an uncertainty of 3%.

The pressure field evolution, depending on the Thoma number, is obtained in the whole draft tube. Only eight pressure sensors in the cone will be presented in this paper, corresponding to the positions described in Fig. 2.

2.4 Data Post Processing. For periodic flows, the signal is reconstructed by synchronizing the acquisition with a reference signal at several time shifts τ—Fig. 4. The reference signal comes from a pressure sensor and the pressure drop corresponding to the vortex passage is used for triggering all acquisitions.

Thus the periodic signal can be decomposed according to

$$C_i(t) = \bar{C} + \tilde{C}(\tau) + C'(t) \tag{1}$$

The phase-locked component $\tilde{C} + \bar{C}$ is obtained by averaging the instantaneous values at the same τ value; see Eq. (3)

$$\bar{C} = \langle C_i \rangle = \lim_{N \to \infty} \frac{1}{N} \sum_{i=1}^{N} C_i(t) \tag{2}$$

$$\tilde{C}(\tau) = \lim_{N' \to \infty} \frac{1}{N'} \sum_{i=1}^{N} [C_i(\tau) - \bar{C}] \tag{3}$$

with

$$\bar{\tilde{C}} = 0$$

$$\langle C' \rangle = \lim_{N \to \infty} [C_i(t) - \bar{C} - \tilde{C}] = 0 \tag{4}$$

Fifteen phase values, equidistant in a vortex passage interval, T_r, are selected to complete the phase average. Thus the vortex synchronous flow is reconstituted.

The LDV acquisition is triggered with the wall pressure signal breakdown given by the vortex passage. The LDV data signal is not continuous, thus an additional reference signal is taken from an optical encoder mounted to the runner shaft. The resolution of the optical encoder is 0.04 deg of runner rotation. In this way we
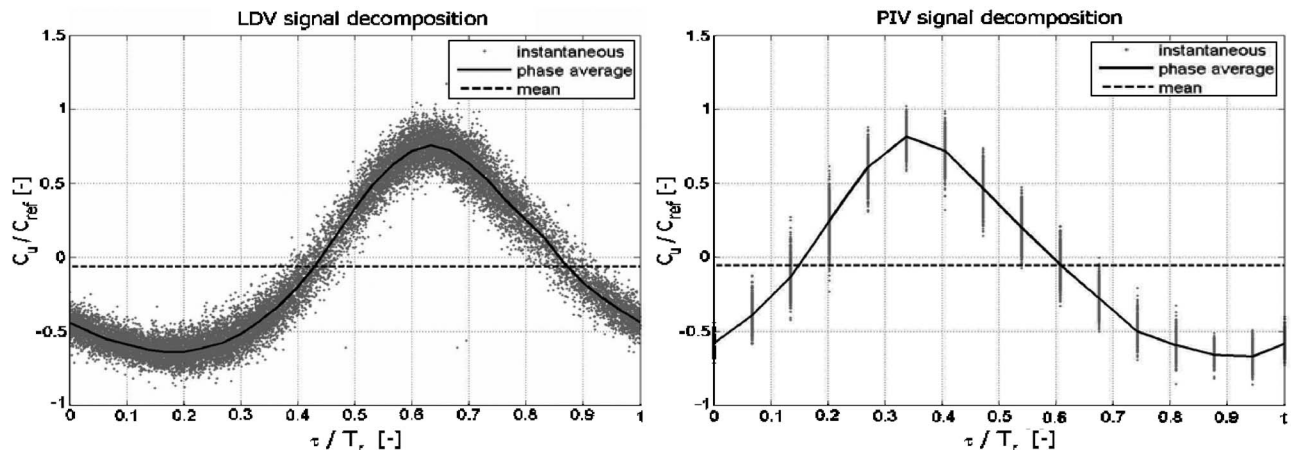

Fig. 4 Phase average calculation of the LDV and PIV velocity signal
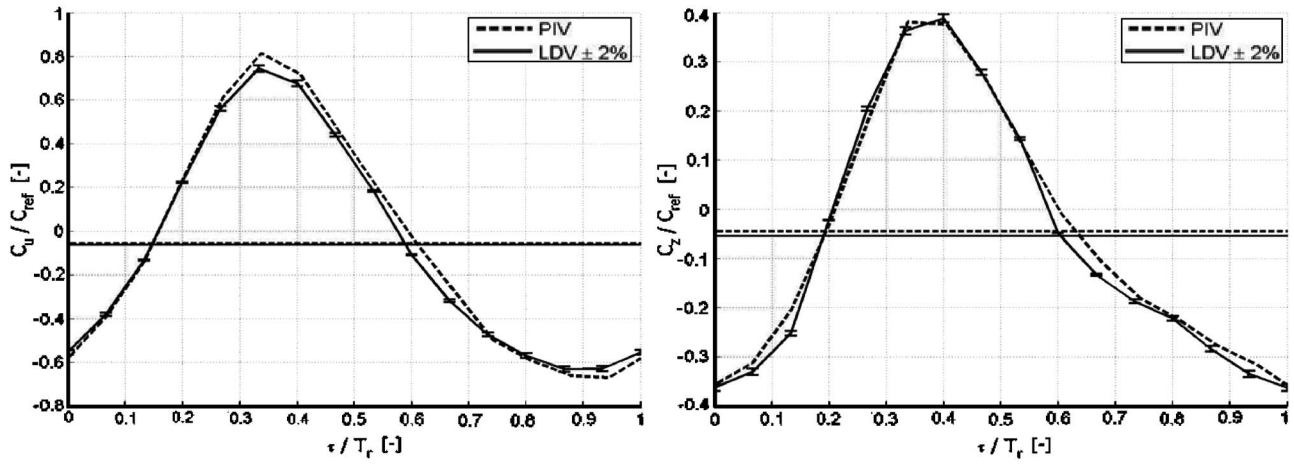
Fig. 5   LDV-PIV phase average comparison

have the relation between the runner spatial position and the vortex period. Thus each LDV acquisition is reported to the corresponding vortex period via the runner position—see Fig. 4. In this way the fluctuation of the vortex period is obtained at 3% of its mean value.

Subsequent to a mean convergence study, the number of acquired velocity values for each phase, τ value, has been between 1000 and 3000 instantaneous values, thus the mean velocity value $\bar{C}$ represents the statistic over 30,000 instantaneous velocity values.

For the PIV measurements, subsequent to a mean convergence study, the number of acquired vector maps for each phase, τ value, has been set to 1200, thus the mean velocity value $\bar{C}$ represents the statistic over 18,000 instantaneous velocity fields. The PIV

acquisition is performed at constant τ value reported to the vortex trigger signal—see Fig. 4. The influence of the vortex period variation for this kind of phase average calculation is checked and fits within the same uncertainty range like the measurement method 3%—see Fig. 5.

The direct comparison between the mean velocity values, see Fig. 12, or phase average velocity values, see Fig. 5, obtained by LDV and PIV measurements in the upper part of the cone, shows an excellent agreement as well.

Concerning the phase average calculations for the unsteady pressure acquisition—at constant acquisition rate—and for the numerical results, they are performed by averaging the instantaneous values for each τ interval.

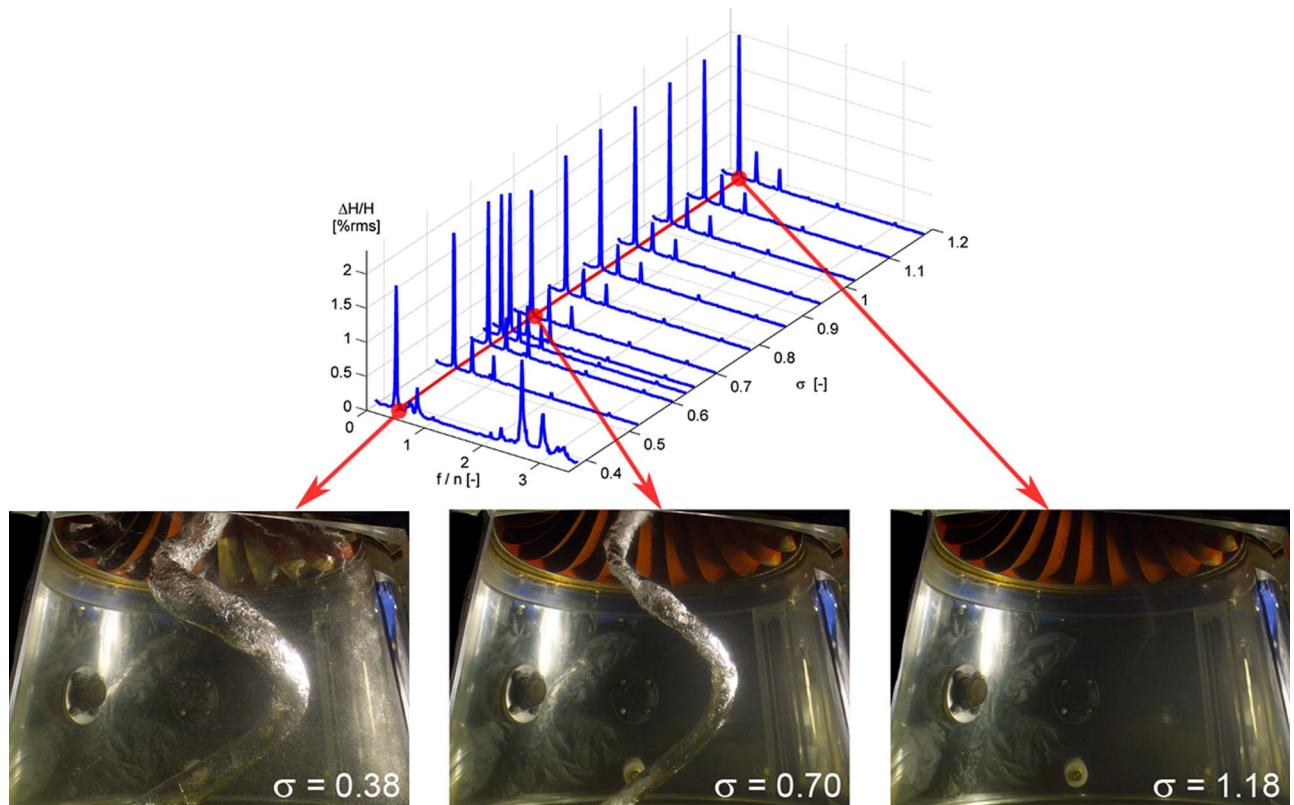**2.5   Description of the Study Case.** The experimental inves-

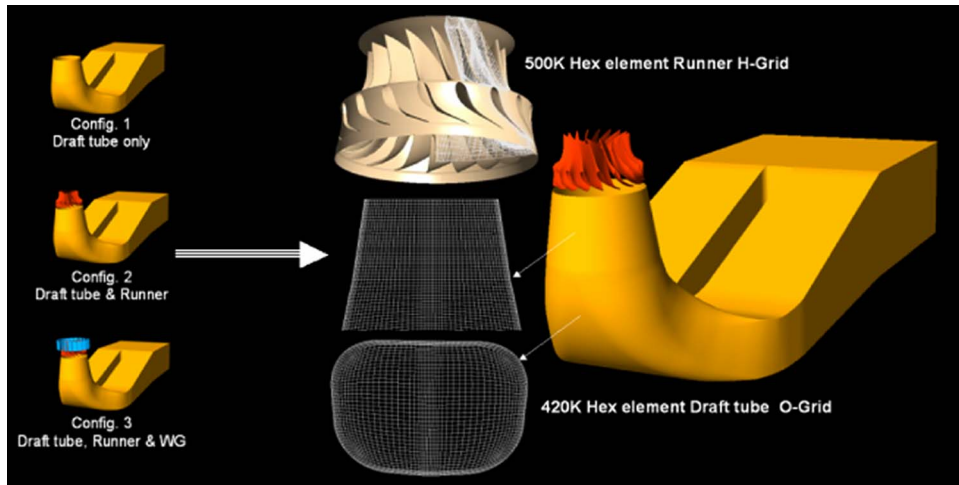**Fig. 6   Waterfall diagram and corresponding cavitation ropes**

Fig. 7 Computation flow domain and mesh

tigation is carried out for a range of Thoma cavitation numbers varying from $\sigma=1.18$, cavitation free conditions, to $\sigma=0.38$, maximum rope volume. For a given operating point, same head and flow rate, the vortex frequency, pressure pulsation amplitude and volume of vapor in the vortex core are dependent of the σ value as shown on the waterfall diagram in Fig. 6.

Since, for the moment, the numerical simulation is performed for single-phase flow condition, the study case is limited to the cavitation free condition, $\sigma=1.18$. The present operating point corresponds to a flow coefficient $\varphi=0.26$ and a specific energy coefficient $\psi=1.18$.

3 Numerical Simulation of Unsteady Flow Behavior

3.1 CFD Methodology for the Unsteady Simulation of the Rotating Vortex. Nowadays it became common to predict flow behavior and energy loss in hydraulic turbine components by CFD application, using a Navier–Stokes flow solver closed with the k-epsilon turbulence model. When individual hydraulic components are optimized, then steady state stage flow analysis for combined hydraulic components is performed to establish the efficiency of the entire turbine—see Vu et al. [3]. For investigation of unsteady flow behavior in hydraulic turbine components, such as the rotating rope phenomena in draft tubes at partial flow rate condition or the interaction of flow between wicket gates and runner blades, unsteady flow computation is required. For the present application, ANSYS-CFX 5.6 version is used for the computation. Also the standard k-epsilon turbulence model is used for the flow simulation.

3.2 Choice of Computational Flow Domain. For the unsteady flow simulation of the rotating vortex rope, there are three possible configurations for the computational flow domain. The first configuration considers only the draft tube geometry. The second configuration includes runner and draft tube, and the third one includes wicket gates, runner, and draft tube geometries. The second configuration is selected here for the unsteady simulation as the best compromise between solution accuracy requirements and computer resources. The transient runner/draft tube simulation allows us to predict the true unsteady interaction of the flow between the upstream runner and the elbow draft tube. In this approach, the unsteady relative motion between the two components on each side of the general grid interface (GGI) connection is simulated. The interface position is updated for every time step, as the relative position of the grids on each side of the interface changes. Figure 7 represents the computational flow domain for the unsteady flow simulation and the multi block structured meshes generated for the runner and the draft tube. An O type

420,000 node mesh is used for the draft tube and an H mesh type with 500,000 nodes is generated for the 17 flow passages of the runner. Due to a foreseen requirement of very large Central Processing Unit (CPU) time for the computation, we prefer to keep a relatively coarse mesh size for the application.

3.3 Computational Procedure for Unsteady Flow Simulation. Two preliminary steady state calculations were performed, the first one for the spiral casing and the distributor, and the second one for the stay vane, guide vane, and runner assembly. The results of the first calculation were used as inlet conditions for the second calculation. In turn, the inlet conditions for the unsteady calculation—including turbulent kinetic energy and dissipation rate profiles—were extracted form the second steady state calculation. The average turbulence intensity at inlet to the unsteady calculation domain is about 3.5% while the average relative viscosity is 110. In this way, for the unsteady computational domain—runner and draft tube—the flow rate, flow direction, and the turbulence intensity obtained in the second steady preliminary calculation are specified as the inlet boundary conditions. The outlet condition is the zero gradient condition in the outflow direction is applied for all variables.

Since we are interested in simulating a periodic-in-time quasi-steady state, it is recommended to first obtain a steady state solu-
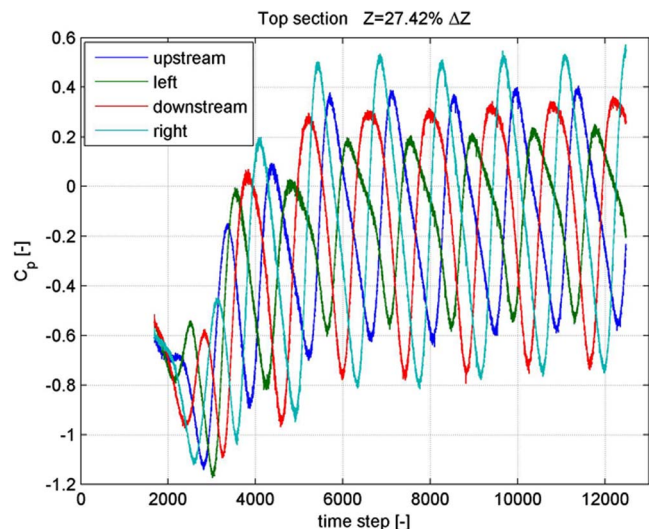

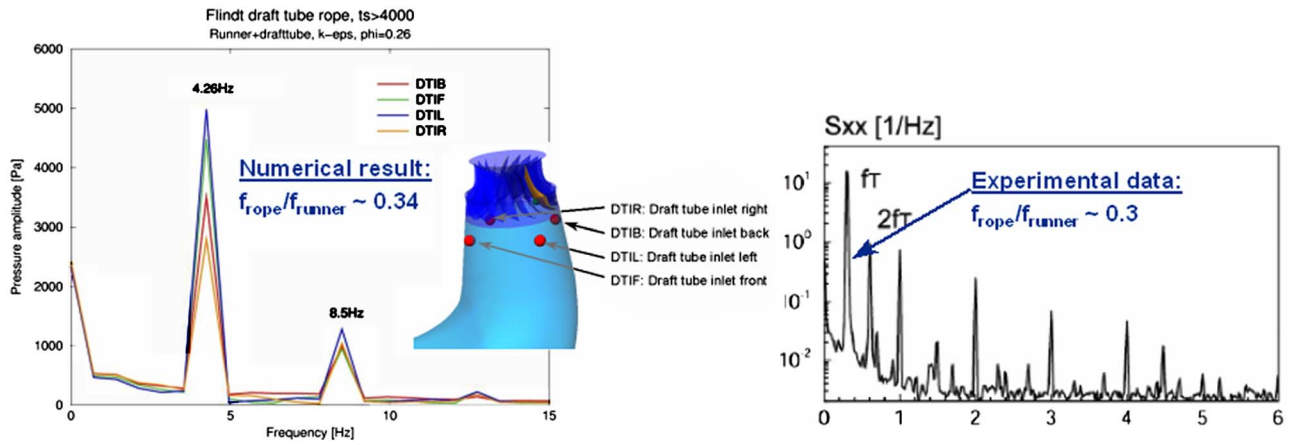**Fig. 8 Evolution of pressure monitoring in transient computation**

Fig. 9 Comparison of CFD and experimental frequency spectra

tion using the stage flow calculation and then using this steady state solution to start the unsteady runner/draft tube simulation. The transient solution should converge to the desired periodic behaviour after several runner revolutions. For hydraulic turbine machines, using time step of about 1 time step /deg of revolution is satisfactory. The rms convergence criterion of the residual for each time step is specified to 10^{-4}. Figure 8 shows the evolution of pressure monitoring in the draft tube cone during the transient

computation. It takes about 1000 time steps to start the fluctuation from a steady state solution and another 3000 time steps to reach the periodic unsteady state. Then starting from that point, we obtain a periodic signal at the cone region as shown in Fig. 8. The numerical solution is considered to be well converged after 11,500 time steps or after 24 runner revolutions. The computation is carried out on a Beowulf Linux cluster. It takes about 25 CPU day time in parallel computing with 4 CPUs.
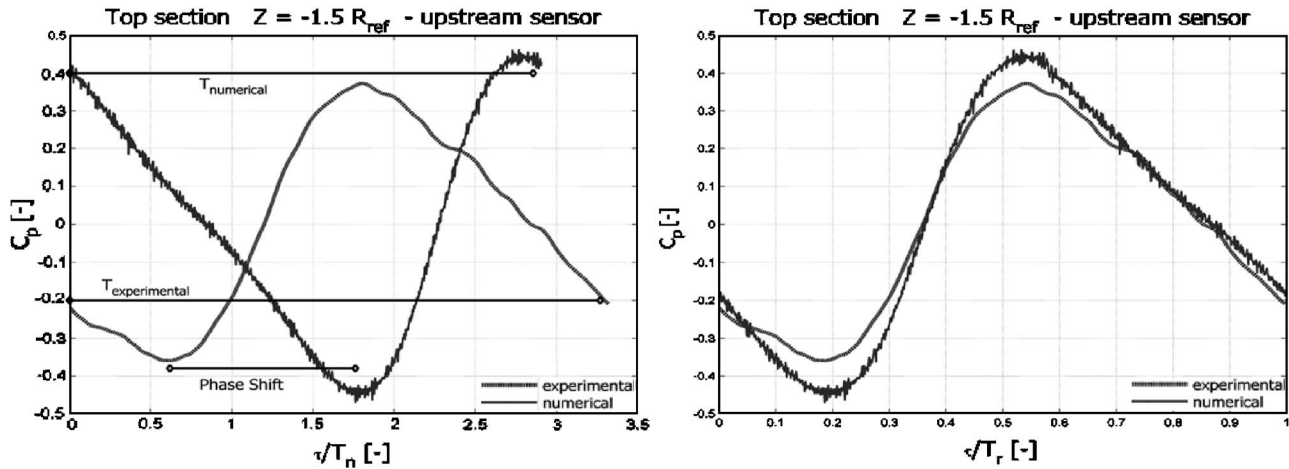

Fig. 10 Period adjustment and phase shift on the numerical data to compare with the experimental ones
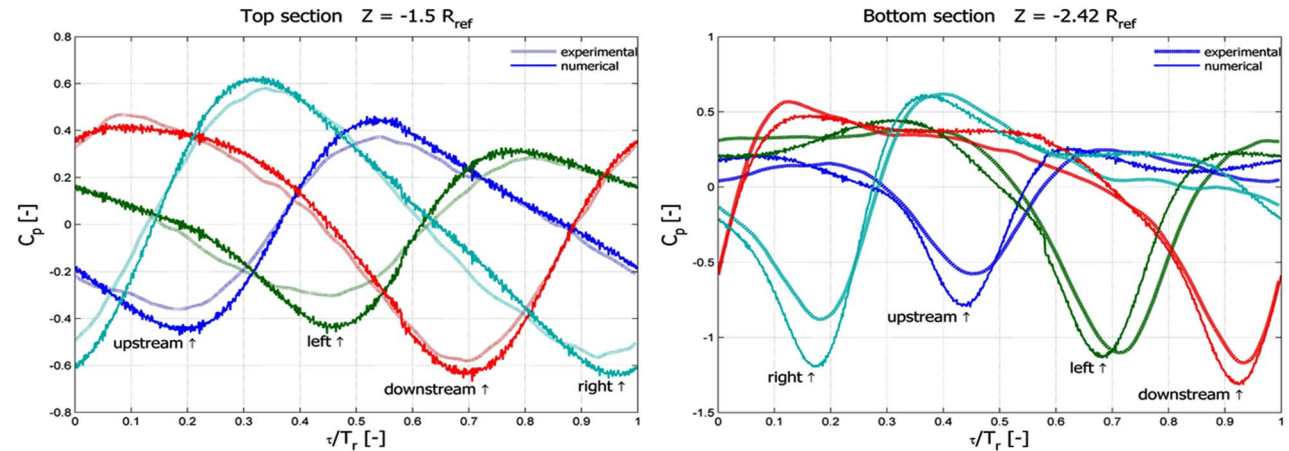

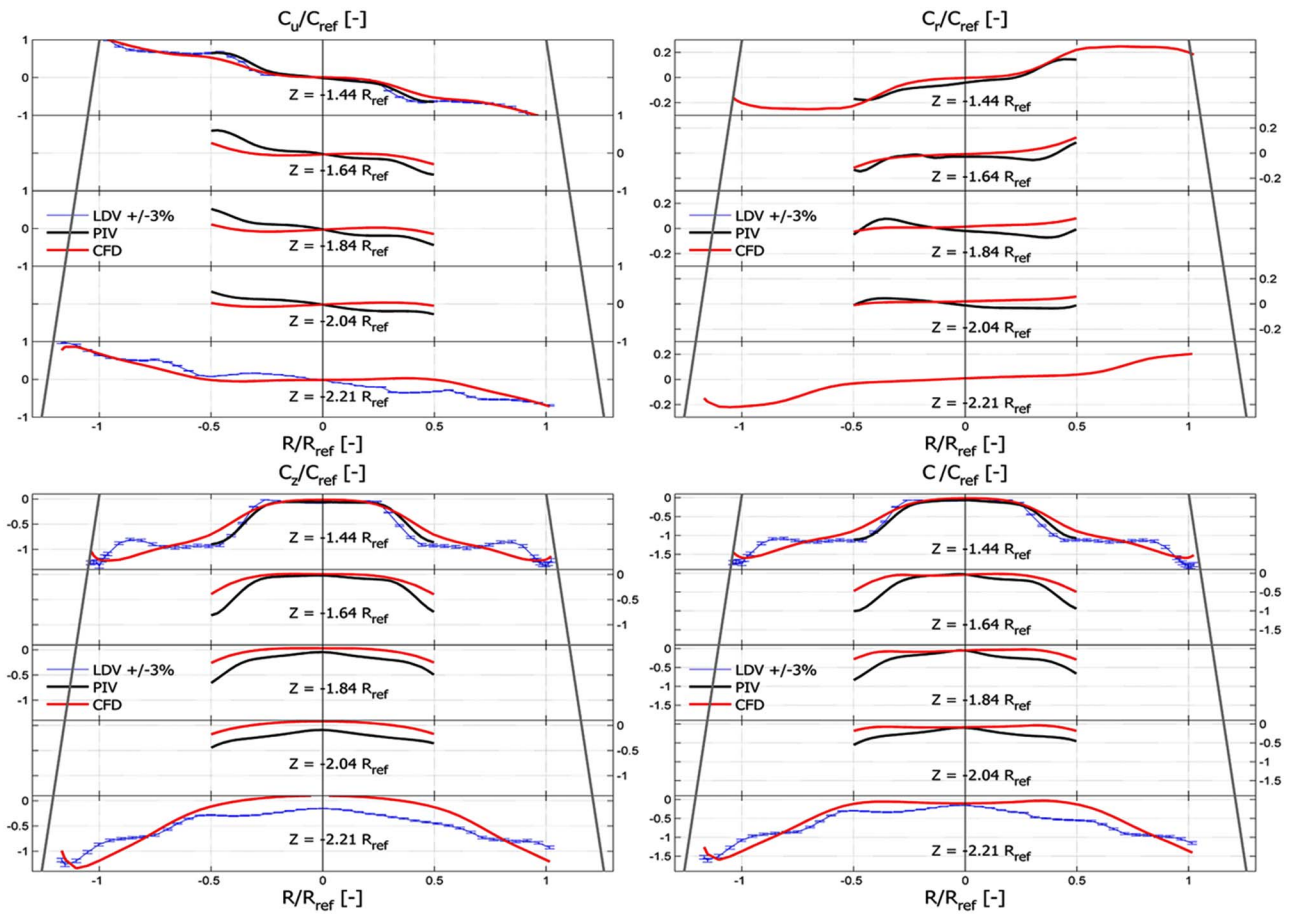**Fig. 11 Phase average wall pressure comparison**

Fig. 12   Mean velocity profiles comparison in the cone

Unsteady flow computations generate tremendous amounts of data if one wants to write a transient solution for every single time step. It is preferable that monitoring points are specified at locations of interest during the preprocessing stage and only intermediary transient solutions are written at a certain interval time step. For the present application, during the last 2500 time steps, monitor points are specified for all locations at which pressure and velocity components (PIV) are measured for a total of about 1200 points. Also, transient solutions are written for every ten time steps.

4   Comparison of the Numerical Solution With Experimental Data

4.1   Validation With Global Quantities. For the partial flow rate operating points, the determining parameters for the interaction between the machine and the circuit are the vortex frequency and the associated pressure amplitude pulsations. The waterfall diagram, as shown in Fig. 6, gives a three-dimensional representation of the pressure fluctuation amplitude spectra in the frequency domain for each σ value. This frequency varies between 0.3 and 0.36 of the runner revolution frequency for the σ investigation range.

4.1.1   Vortex Frequency. For $\sigma = 1.18$, the vortex frequency from the experimental data is 0.30 of the runner revolution. The numerical vortex frequency obtained by frequency spectrum analysis is 0.34 of the runner revolution frequency—see Fig. 9. Thus the numerical simulation vortex frequency is about 13% higher than the measured vortex frequency but it falls within the measured variation range for the σ values in these operating conditions.

4.1.2   Pressure Fluctuation Amplitude. For comparing the phase average pressure fluctuation resulting from the numerical calculation with the experimental results, the phase reference of the numerical simulation is adjusted in order to match the phase of the experimental signal. Therefore, the phase reference is chosen for an experimental sensor: all the others begin synchronized with this one. The numerical phase—without any physical significance—is adjusted on the position of the experimental sensor and all numerical phase averages are corrected with this phase shift (difference) $\delta\tau$—see Fig. 10.

To be coherent for the period representations, the experimental period was chosen like reference and the numerical period is stretched to a dimensionless vortex period as follows:

$$\tau = \tau_{\text{Numerical}} - \delta\tau$$

$$k_r = \frac{T_{r\text{Numerical}}}{T_{r\text{Experimental}}} \tag{5}$$

$$\tau = \tau_{\text{Experimental}} \cdot k_T$$

Figure 2 shows monitor points for static pressure at different section planes. Figure 11 shows the comparison of the numerical static pressure fluctuation with the experimental data for one period of the vortex. Both signals are normalized with their own vortex frequency. The correlation between the numerical simulation and the experimental data is excellent. The pressure fluctuation amplitude is well predicted not only at the runner outlet, but its evolution in the cone is in good agreement with the experimental data for all sensors angular positions, as well—see Fig. 2. The
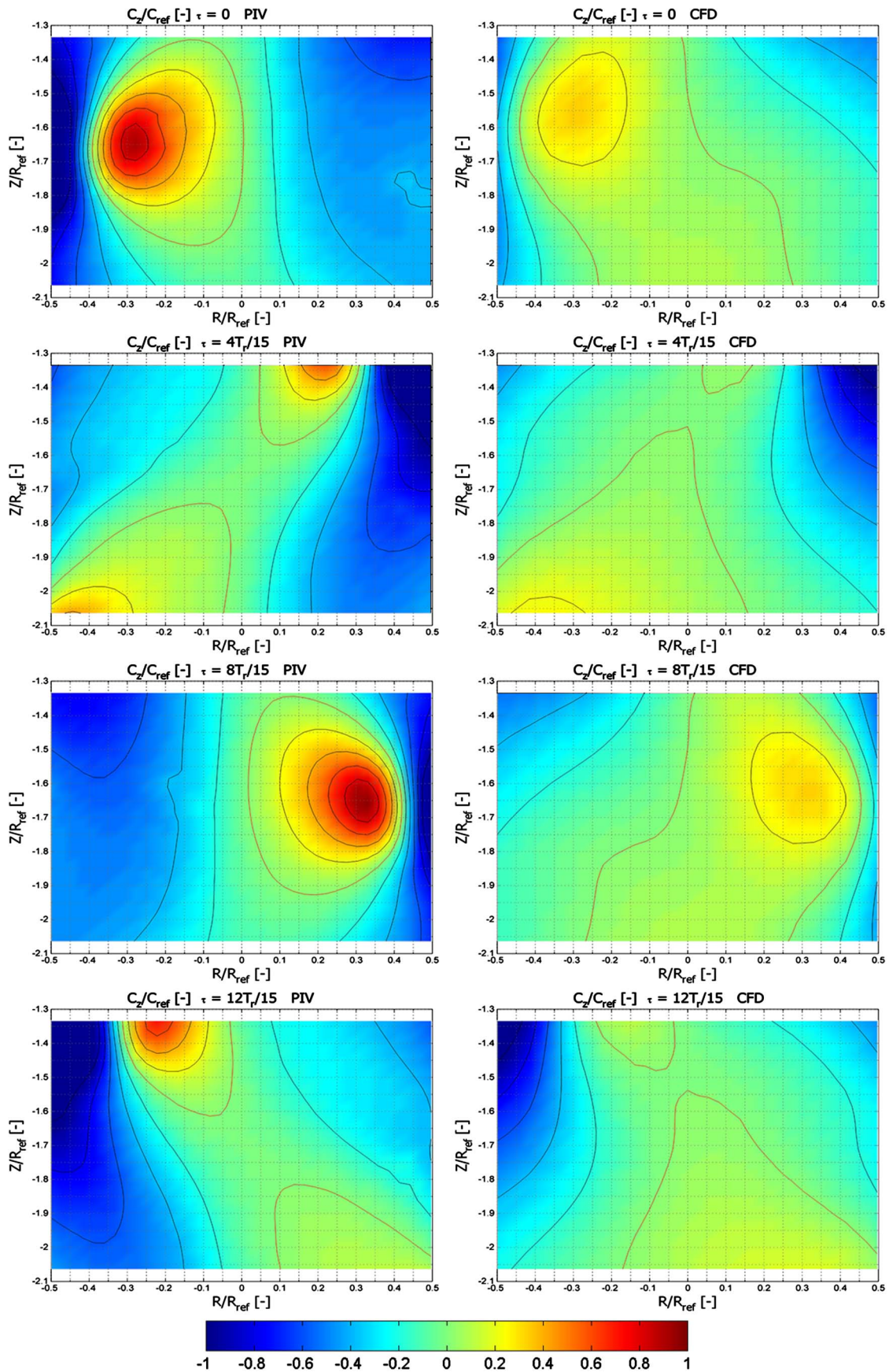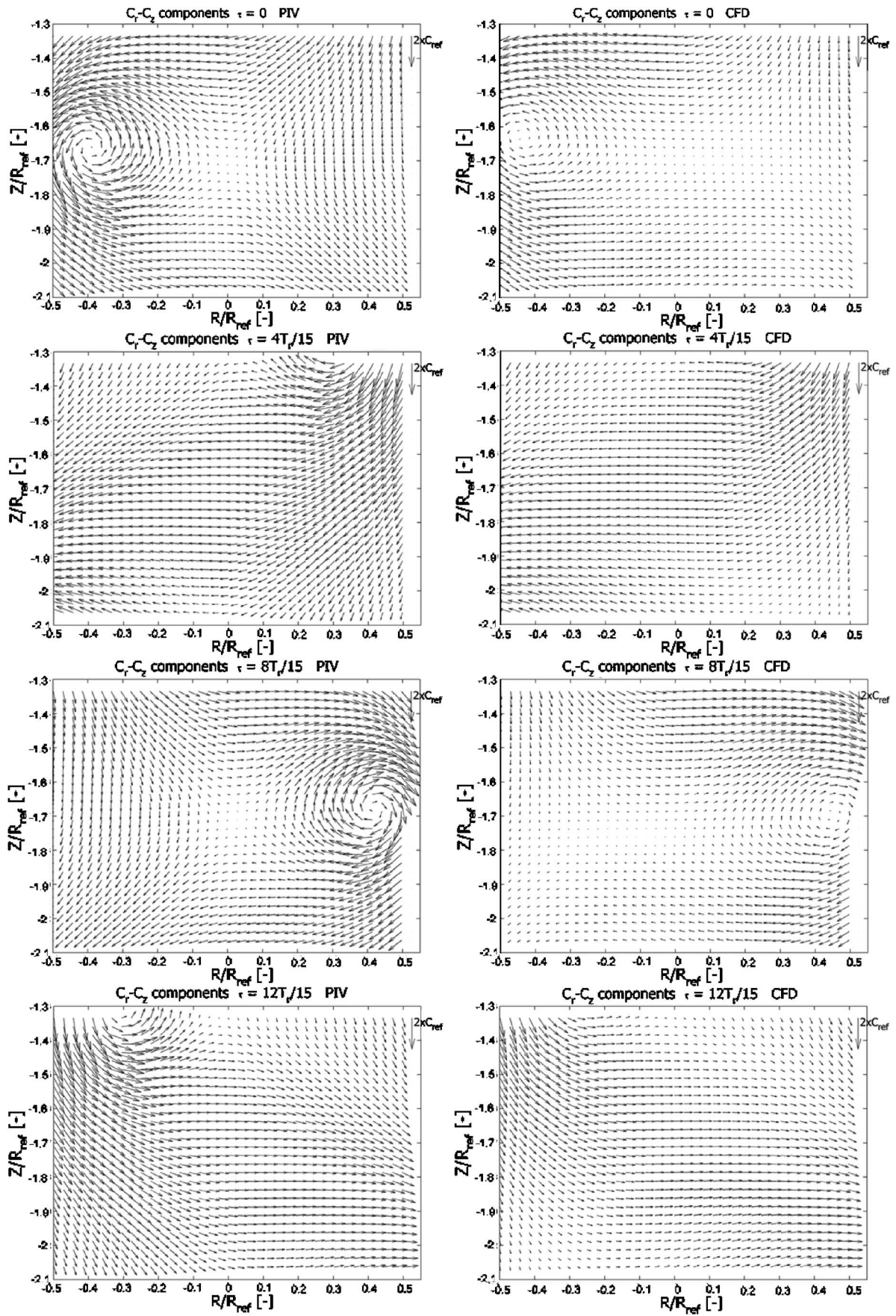
Fig. 13 C_z phase average velocity profiles

Fig. 14 C_r - C_z phase average velocity profiles comparison in the cone

difference between the experimental results and numerical ones reported to the mean pressure level is less than 2.5%, so in the same range as the measurement accuracy.

4.2 Validation with Local Flow Structure. For improving the turbines design it is necessary to predict the real flow structure and associated phenomenology throughout the entire analyzed domain.

4.2.1 Mean Velocity Profiles. The mean flow velocity shows the decelerated swirling flow that develops in a central stagnation zone—see Fig. 12. The vortex encloses this zone of average velocity near zero. The flow rate distribution is therefore restricted to the circular zone between the cone walls and the vortex conical supporting surface. The LDV measurements that complete the PIV measurements in the inlet and outlet cone cross sections show a higher velocity near the cone wall, for the axial and tangential velocity. The angle at which the stagnation region develops downstream is higher than the angle of the turbine cone.

For assessing the flow structure prediction, the numerical mean velocity field is compared with the LDV and PIV measurements. The comparison of the flow structure in the cone of the turbine shows a generally good agreement of the velocity mean values—see Fig. 12. A small difference is observed at the runner outlet in the strong velocity gradients zone—between $R/R_{out}=0.2$ to 0.35. The numerical results are smoother, and for this reason the zone of the mean near zero velocities, in the centre of the cone, is not the same.

4.2.2 Phase Average Velocity Field. For the comparison of LDV and PIV velocity measurements with the CFD results, the same procedure like for the pressure is considered: the numerical period is shifted onto the experimental one and the same phase shift $\delta\tau$ is applied for all numerical velocity signals.

The central stagnation zone, observed in the time averaged values, represents the zone closed by the vortex passage in phase average values. This region is a series of backflows, triggered by the vortex passage—see Fig. 13.

The phase average vector field representation shows the vortex position in the measurement section—see Fig. 14. The phase correspondence obtained by the pressure fitting is the same as for the phase velocity profiles. Qualitatively the vortex center position is placed on the same cone height. A small difference is observed in the radial position, in the numerical simulation, it is closer to the cone wall. This difference is in accordance with the mean velocity profile. The phase average flow structure of the numerical simulation is very similar to the experimental measurements one.

4.2.3 Vorticity Field. The calculation of the vorticity—see Eq. (6), for each phase averaged velocity field, permits to quantify the vortex evolution in the measurement zone.

$$\vec{\Omega} = \vec{\nabla} \times \vec{C} \qquad (6)$$

As represented in Fig. 15, the vortex position is well predicted by the numerical calculations, with a difference of 5% of the radius between the predicted position and the measured one. The vorticity is smaller in numerical calculations with about 18%, but its position closer to the cone walls explains the fact that the same pressure fluctuation amplitude values are obtained at the wall.

4.2.4 Vortex Center. The vortex center position is estimated considering the vortex center as the maximum vorticity point in the cone section which corresponds to the stagnation point in the phase average flow field—see Fig. 16. The vortex position trace in the section is similar with the rope position visualization by the vapors zone in the section for the low sigma numbers—see Fig. 6. The comparison of the vortex center between experimental and numerical data is representative for the vortex phenomenology and the difference between the center position, as well as the vorticity intensity, could by explained by the relatively coarse
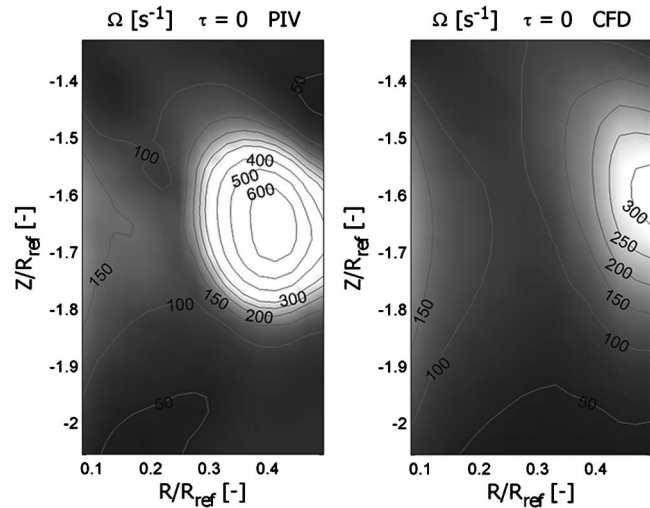
mesh compared to the vortex size—see Fig. 17. The mesh size is chosen as the best compromise between the result quality and the required computational time.

5 Concluding Remarks

This paper has presented a CFD methodology to study the unsteady rotating vortex in the FLINDT draft tube and associated experimental study of the flow phenomena.

A large experimental database is built in the frame of the FLINDT project for partial flow rate operating regime. 3D PIV, 2D LDV, unsteady wall pressure, and unsteady wall friction measurements are available for analysis, with certified accuracy.

The transient flow simulation is for single phase using a standard k-epsilon turbulence model. Although a relatively coarse mesh is used for the computational, an excellent agreement between numerical results and experimental data is obtained. The accuracy of the prediction for the vortex global quantities, pressure pulsation amplitude (3% error), and vortex frequency (13% error) is very good. For the first time the simulated vortex structure of the rotating vortex is assessed and compared with experimental measurements. The quantitative analyses in terms of mean velocity field, phase average velocity field, vorticity, and vortex center position also show a good agreement and validate the phenomenology of the vortex rope in numerical simulations. We can
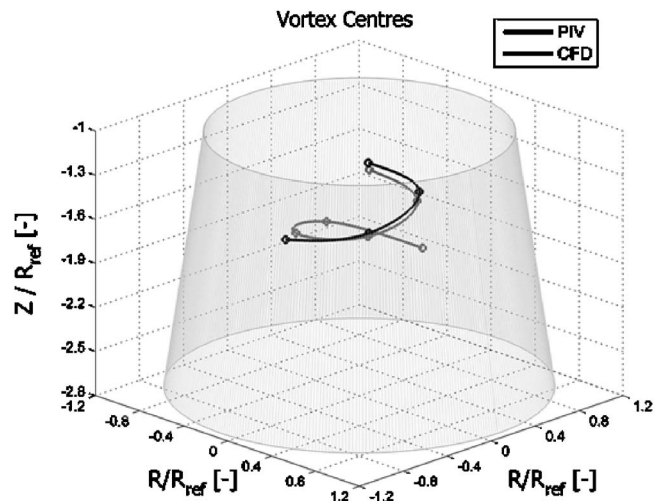

Fig. 15 Vorticity field in the cone

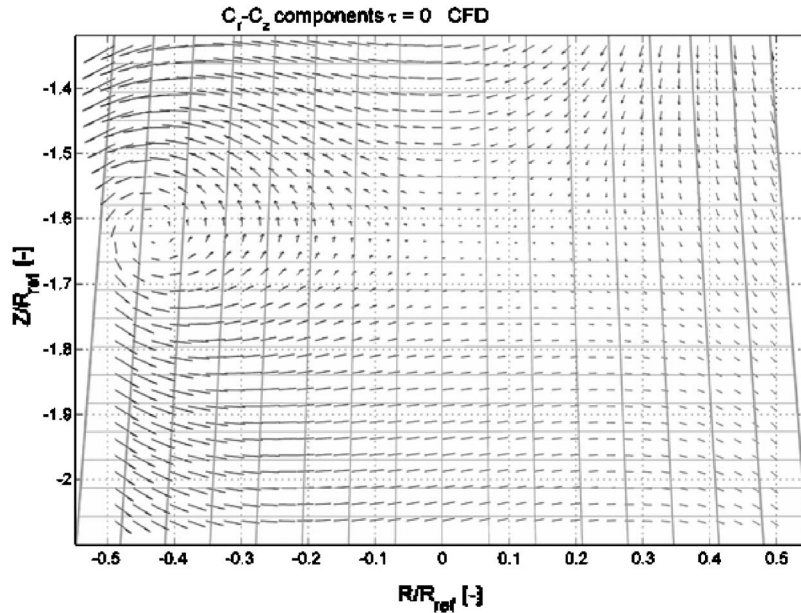**Fig. 16 Vortex center evolution in the cone**

Fig. 17 Mesh size in the vortex center position

use with confidence this approach for design purpose application. Compared with a classical steady simulation, the unsteady CFD used for partial flow rate simulation provides important information for the machine design: the wall pressure unsteady fluctuations level and velocity field structure.

In the future the extension of this approach to two phase flows will permit to take into account another important parameter for the partial flow rate phenomenology: the cavitation and its compliance.

Acknowledgment

Nomenclature

E = specific energy (J/kg)
Q = flow rate (m³/s)
Q_{BEP} = flow rate at the best efficiency operating condition (m³/s)
σ = cavitation number
$D_{\bar{1}e}$ = runner diameter (m)
C_i = instantaneous velocity (m/s)
$\tilde{C}$ = periodic fluctuating component (m/s)
$\bar{C}$ = time-averaged velocity value (m/s)
C' = random turbulent fluctuation (m/s)
C_u = tangential component (m/s)
C_z = axial component (m/s)
C_r = radial component (m/s)
C = absolute velocity (m/s)

C_{ref} = mean flow reference velocity $C_{ref}=Q/A$(m/s)
ψ = specific energy coefficient
φ = flow rate coefficient
C_p = pressure coefficient $C_p=(p-\bar{p})/1/2\rho c_{m\bar{1}}^2$
ω = rotational velocity (rad/s)
ΔZ = cone height (m)
Z = cone's current depth (m)
R = local cone radius (m)
R_{out} = cone outlet radius (m)
f_r = vortex rotation frequency (Hz)
n = runner rotation frequency (Hz)
τ = phase delay (s)
θ = angular position of the vortex $\theta=2\pi\tau f_r$ (rad)
T_n = runner rotation period (s)
T_r = vortex rotation period (s)
BEP = best efficiency operating point
Re = re number Re$=UD/\nu=\pi ND^2/60\nu$

References

[1] Jacob, T., 1993, "Evaluation sur Modèle Réduit et Prédiction de la Stabilité de Fonctionnement des Turbines Francis," EPFL Thesis No. 1146, Lausanne, Switzerland.
[2] Nishi, M., Matsunaga, S., Kubota, T., and Senoo, Y., 1984, "Surging Characteristics of Conical and Elbow-Type Draft Tubes," in *Proceedings of the 12th IAHR Symposium*, pp. 272–283.
[3] Vu, T. C., and Retieb, S., 2002, "Accuracy Assessment of Current CFD Tools to Predict Hydraulic Turbine Efficiency Hill Chart," *Proceedings of the 21st IAHR Symposium on Hydraulic Machinery and Systems*, Lausanne, Switzerland, pp. 193–198.
[4] Ruprecht, A., Maihöfer, M., Heitele, M., and Helmrich, T., 2002, "Massively Parallel Computation of the Flow in Hydo Turbines," *Proceedings of the 21st IAHR Symposium on Hydraulic Machinery and Systems*, Lausanne, Switzerland, pp. 199–206.
[5] Ruprecht, A., Helmrich, T., Aschenbrenner, T., and Scherer, T., 2002, "Simulation of Vortex Rope in a Turbine Draft Tube," *Proceedings of the 21st IAHR Symposium on Hydraulic Machinery and Systems*, Lausanne, Switzerland, pp. 259–266.
[6] Scherer, T., Faigle, P., and Aschenbrenner, T., 2002, "Experimental Analysis and Numerical Calculation of the Rotating Vortex Rope in a Draft Tube Operating at Part Load," *Proceedings of the 21st IAHR Symposium on Hydraulic Machinery and Systems*, Lausanne, Switzerland, pp. 267–276.
[7] Miyagawa, K., Tsuji, K., Yahara, J., and Nombra, Y., 2002, "Flow Instability in an Elbow Draft Tube for a Francis Pump-Turbine," *Proceedings of the 21st IAHR Symposium on Hydraulic Machinery and Systems*, Lausanne, Switzerland, pp. 277–286.
[8] Sick, M., Dorfler, P., Michler, W., Salllaberger, M., and Lohmberg, A., 2004,

"Investigation of the Draft Tube Vortex in a Pump-Turbine," *Proceedings of the 22nd IAHR Symposium on Hydraulic Machinery and Systems*, Stockholm, Sweden.

[9] IEC 60193 Standard, 1999, "Hydraulic Turbines, Storage Pumps and Pump-Turbines-Model Acceptance Tests," International Electrotechnical Commission, Genève, Switzerland.

[10] Iliescu, M. S., Ciocan, G. D., and Avellan, F., 2002, "3D PIV and LDV Measurements at the Outlet of a Francis Turbine Draft Tube," Joint U.S. ASME—European Fluids Engineering Summer Conference, Montreal, Quebec, Canada,

Paper No. FEDSM2002-31332.

[11] Ciocan, G. D., Avellan, F., and Kueny, J. L., 2000, "Optical Measurement Techniques for Experimental Analysis of Hydraulic Turbines Rotor-Stator Interaction," ASME Fluid Engineering Conference, Boston, Paper No. FEDSM2000-11056.

[12] Arpe, J. A., and Avellan, F., 2002, "Pressure Wall Measurements in the Whole Draft Tube: Steady and Unsteady Analysis," *Proceedings of the 21st IAHR Symposium on Hydraulic Machinery and Systems*, Lausanne, Switzerland.